https://doi.org/10.1038/s41586-019-1149-8

Twentieth-century hydroclimate changes consistent with human influence

Kate Marvel[1,2,5]*, Benjamin I. Cook[1,5], Céline J. W. Bonfils[3], Paul J. Durack[3], Jason E. Smerdon[4] & A. Park Williams[4]

Although anthropogenic climate change is expected to have caused large shifts in temperature and rainfall, the detection of human influence on global drought has been complicated by large internal variability and the brevity of observational records. Here we address these challenges using reconstructions of the Palmer drought severity index obtained with data from tree rings that span the past millennium. We show that three distinct periods are identifiable in climate models, observations and reconstructions during the twentieth century. In recent decades (1981 to present), the signal of greenhouse gas forcing is present but not yet detectable at high confidence. Observations and reconstructions differ significantly from an expected pattern of greenhouse gas forcing around mid-century (1950–1975), coinciding with a global increase in aerosol forcing. In the first half of the century (1900–1949), however, a signal of greenhouse-gas-forced change is robustly detectable. Multiple observational datasets and reconstructions using data from tree rings confirm that human activities were probably affecting the worldwide risk of droughts as early as the beginning of the twentieth century.

Tree ring records can be used to reconstruct temperature and hydroclimatic variables at annual and seasonal resolutions. Over the last several decades, large networks of these records have been used to target gridded reconstructions of the Palmer drought severity index (PDSI), a widely used indicator of soil moisture variability that is typically averaged over the summer months (June–July–August or December–January–February in the Northern and Southern Hemispheres, respectively) during the active growing season. These efforts have yielded 'drought atlases' of North America (North American drought atlas, NADA)[1,2], Europe and the Mediterranean (Old World drought atlas, OWDA)[3], Mexico (Mexican drought atlas, MXDA)[4], monsoon Asia (monsoon Asian drought atlas, MADA)[5], and Australia–New Zealand (Australia and New Zealand drought atlas, ANZDA)[6]. Drought atlases provide a comprehensive picture of regional soil moisture that dates back centuries: high-quality information exists in the MXDA, ANZDA and MADA from AD 1400 to present, while the NADA and OWDA provide reasonably comprehensive regional coverage dating back to AD 1100. These drought atlases have been used to validate general circulation models[1], understand the climate context of current[7,8] and historical[9] events, and identify past megadroughts[2]. Here we use the collection of drought atlases for a dual purpose: to understand recent changes in soil moisture during the twentieth and twenty-first centuries, during which time anthropogenic radiative forcing has steadily been increasing, and to estimate naturally forced and internal variability in the preindustrial era.

PDSI is a standardized index, in which values of zero represent the baseline average conditions and positive or negative values indicate wet or dry departures from the baseline climatology. Despite its widespread and effective use[10], valid criticisms have been raised about the use of PDSI as an indicator of drought[11–14] (see Methods). We therefore test the sensitivity of our results to PDSI wherever possible by conducting additional comparisons and analyses using estimates of surface and root-zone soil moisture from coupled climate model simulations[15] (Supplementary Table 2) and observation-constrained land-surface models[16,17].

Expected anthropogenic changes

We use a pattern-based detection and attribution method that was initially developed at Lawrence Livermore National Laboratory ([18–21]). In this model, the expected response to external forcing is calculated by averaging forced model simulations to decrease internal variability, which is expected to be uncorrelated across separate model runs. The 'fingerprint' is then defined as the leading empirical orthogonal function (EOF) of this multi-model average from 1900 to 2099. In this study, we use the 'historical' simulations archived by the Coupled Model Intercomparison Project Phase 5 (CMIP5, Supplementary Table 3) and extended these simulations to 2100 using simulations of the Representative Concentration Pathway 8.5 (RCP8.5). These extended simulations—which we refer to as H85—contain time-varying changes in all natural (volcanic and solar) and anthropogenic (ozone depletion, land-use change, aerosols and greenhouse gases) drivers and are dominated by the large increase in greenhouse gas concentrations[22] at the end of the twenty-first century. Because of this dominance, such fingerprints reflect the primary role of greenhouse gases and can be thought of as the response of the climate to anthropogenic greenhouse gas emissions.

The PDSI fingerprints and associated principal components for the individual drought atlas regions are shown in Fig. 1. Consistent with previous literature[23], the expected fingerprints are characterized by drying across most of North America and Europe and moistening in the Indian subcontinent and western China. The principal components reveal that, in the multi-model average, the individual fingerprints are increasingly present as the twenty-first century progresses. Additionally, the principal components reveal similar twentieth-century trends in most regions in the drought atlases: an initial increase, followed by a mid-twentieth century decrease in all regions except Australia and New Zealand, and a subsequent positive trend towards the end of the twentieth century.

To compare observations and model expectations, we calculate a 'projection' time series that measures the spatial covariance between the data and the fingerprint as a function of time (see Methods). If

[1]NASA Goddard Institute for Space Studies, New York, NY, USA. [2]Department of Applied Physics and Applied Mathematics, Columbia University, New York, NY, USA. [3]Program for Climate Model Diagnosis and Intercomparison, Lawrence Livermore National Laboratory, Livermore, CA, USA. [4]Lamont-Doherty Earth Observatory, Columbia University, Palisades, NY, USA. [5]These authors contributed equally: Kate Marvel, Benjamin I. Cook. *e-mail: kate.marvel@nasa.gov

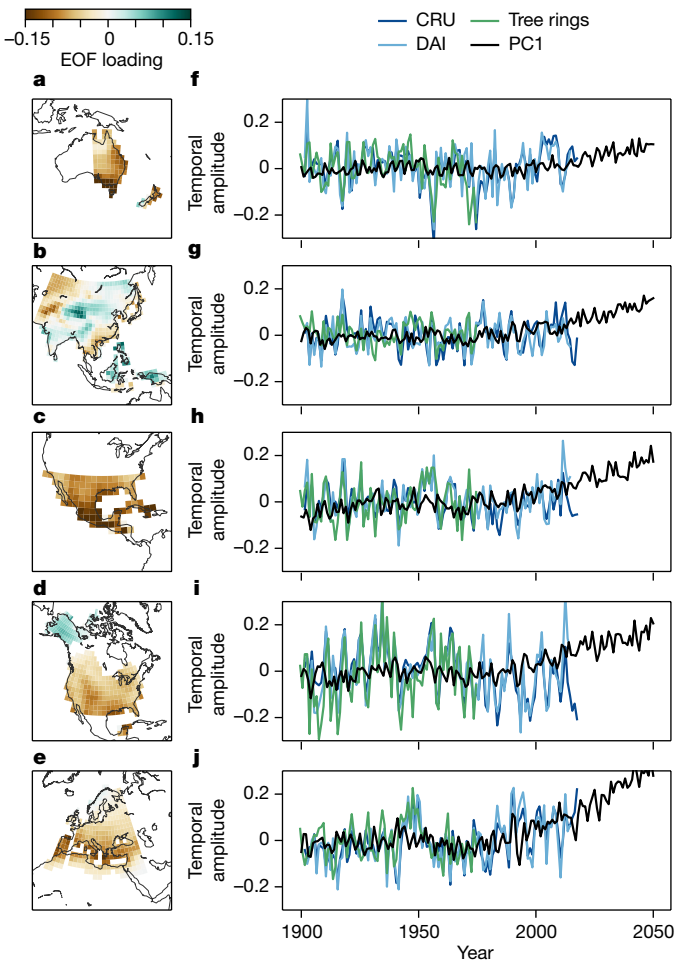

Fig. 1 | Regional fingerprints. a–e, Leading EOFs (fingerprint) of the multi-model mean PDSI from historical and RCP8.5 simulations for ANZDA (**a**), MADA (**b**), MXDA (**c**), NADA (**d**) and OWDA (**e**). **f–j**, The leading principal components (black; PC1) and projections of tree-ring-derived drought atlases (green) and meteorological datasets (light blue for the global PDSI dataset compiled by A. Dai[24,33] and dark blue for the dataset provided by the University of East Anglia Climatic Research Unit, CRU[25]) associated with the fingerprints for ANZDA (**f**), MADA (**g**), MXDA (**h**), NADA (**i**) and OWDA (**j**).

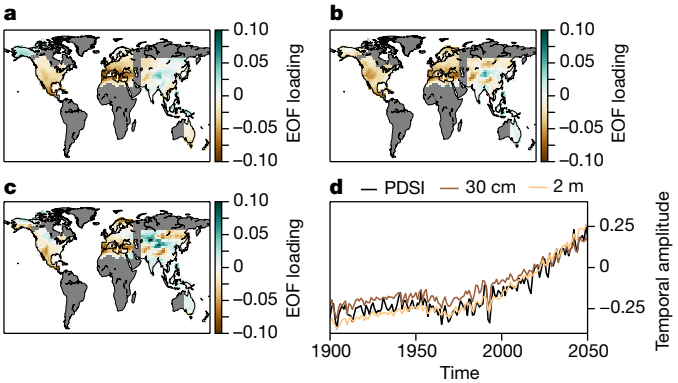

Fig. 2 | Global fingerprints. a–c, Fingerprints for PDSI (**a**), column-integrated soil moisture to 30 cm (**b**) and column-integrated soil moisture to 2 m (**c**), defined as the leading EOF of the multi-model average of H85 for each variable over the 1900–2099 period. **d**, The associated principal components for each of the EOFs in **a–c**. Land areas over which no drought atlas data exist are shaded in grey.

the fingerprint is increasingly apparent in the observations or reconstructions under consideration, this projection will show an upward trend with time; conversely, a negative trend indicates that the data and fingerprint are increasingly dissimilar. We then project the tree-ring-based drought atlases and two additional datasets[24,25] constructed from observations of meteorological variables onto the model-based fingerprints over their respective domains (Fig. 1f–j and Methods). In the MXDA, and particularly in the NADA and OWDA, the tree ring reconstructions show a positive trend at the beginning of the twentieth century: they increasingly resemble the fingerprint. In the middle of the twentieth century, these trends become negative, before becoming positive again in recent decades.

Detection and attribution of externally forced signals is often more challenging at regional scales[26] and a global perspective may result in earlier detection times. However, the most recent Intergovernmental Panel on Climate Change (IPCC) report[10] indicates only low confidence in attributing changes in drought even over global land areas. Previous studies[21,27] have suggested that signal detection is more robust when the fingerprint captures multiple aspects of the forced signal while simultaneously minimizing noise and, by combining data from multiple drought atlases into a single Global Drought Atlas (GDA; see Methods), we expect to improve the signal-to-noise ratio in two ways. First, increasing the land area can increase the signal: simultaneous drying in Australia, Mexico and the Mediterranean, for example, is a stronger signal than drying in any one of those regions in isolation. Second, a global perspective can reduce noise due to internal climate variability. The hydroclimate in Mexico and Australia is highly sensitive to the El Niño/Southern Oscillation (ENSO), but droughts in these regions are associated with opposite phases of the oscillation. Drought conditions in the Mediterranean, by contrast, are relatively unaffected by ENSO and far more sensitive to the North Atlantic Oscillation[28]. This means that it is harder for natural climate variability alone to produce, by chance, simultaneous drying across all three regions that were identified in the fingerprint.

The model-derived PDSI fingerprint over the GDA region is shown in Fig. 2a. For comparison, we also show the fingerprints of soil moisture at the surface (around 30 cm depth; Fig. 2b) and root zone (about 2 m depth; Fig. 2c). The broad, although imperfect, agreement (see Methods) between PDSI and soil moisture suggests that PDSI, despite its simplified nature as a drought indicator[13,14], is broadly consistent in its behaviour compared to the more process-constrained estimates of soil moisture from the coupled models. Notably, the associated principal components (Fig. 2d) all show similar trends over different intervals of the twentieth century: positive during the first half of the twentieth century) (1900–1949), negative from 1950 to 1975 and positive thereafter.

Signal, noise and time of emergence

As typical in the detection and attribution literature, we define the signal $S(L)$ to be the linear trend in the L-length projection time series[18]. This signal is assessed for significance against a 'noise' term that quantifies natural climate variability[19]. In most cases, the signal is estimated from observational datasets[21,29] and climate noise is estimated by projecting the output of general circulation models (GCMs) that were run under unforced preindustrial[20] or past-millennium[30] conditions onto the fingerprint. The standard deviation of all possible L-length trends in this time series $N(L)$ is a standard measure of climate noise. For PDSI, the availability of the drought atlas reconstructions enables us to measure preindustrial variability that is independent of GCMs. The projection of the GDA onto the H85 PDSI fingerprint is shown in Fig. 3a. We use pre-1850 values of this time series to estimate preindustrial internal and naturally forced variability. The amplitude of this noise varies regionally and with trend length L (Extended Data Fig. 1).

The model-predicted 'time of emergence'—the time at which the forced signal is expected to emerge from natural climate variability—is defined as the year in which the average signal in CMIP5 H85 models,

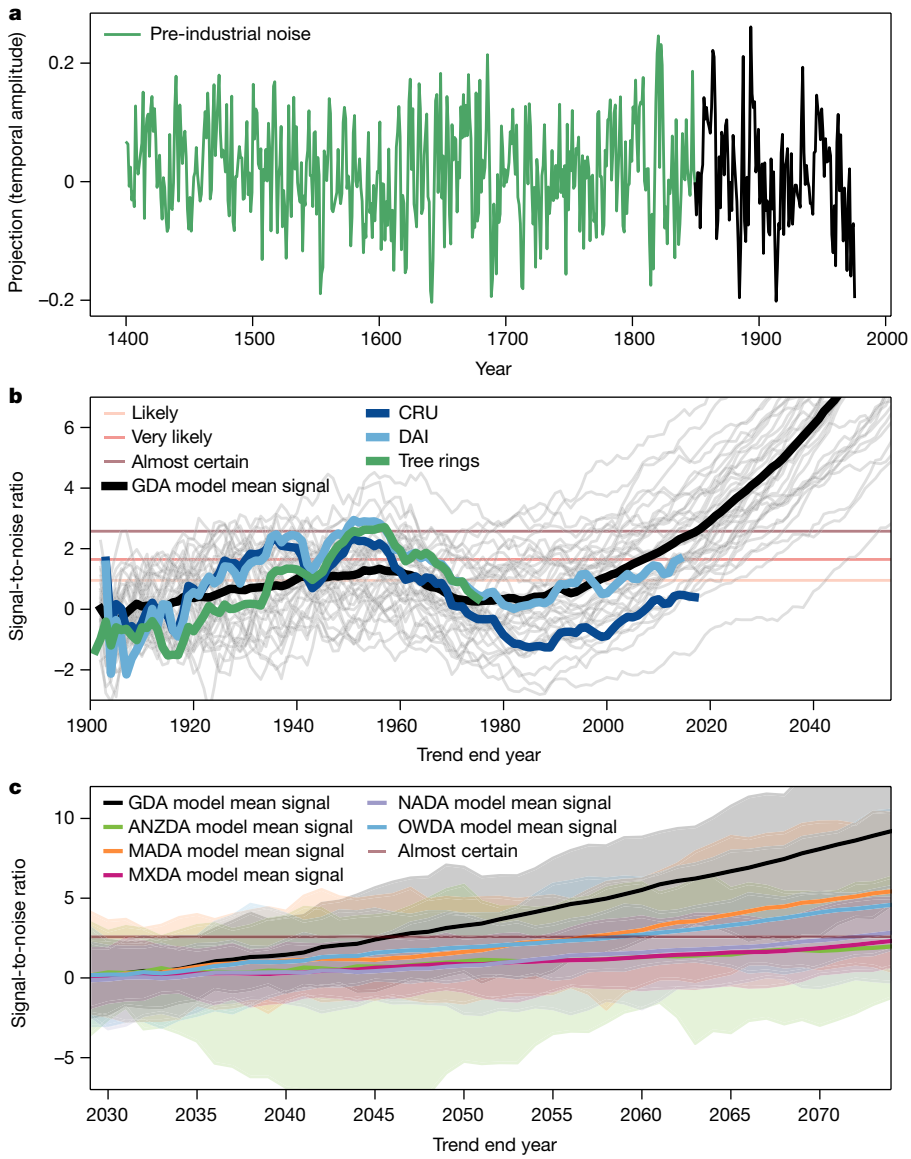

Fig. 3 | Projections and time of emergence. a, Projection of growing season PDSI from the GDA onto the modelled fingerprint shown in Fig. 2a. Preindustrial (pre-1850) variability is shown in green. **b**, Time of emergence for model-predicted and observed signals in PDSI. Horizontal lines correspond to the thresholds of likely ($S/N > 0.95$; detectable at 66% confidence), very likely ($S/N > 1.64$, 90% confidence) and virtually certain ($S/N > 2.57$, 99% confidence). Thin grey lines show the results for individual H85 simulations and the thick black line shows the multi-model mean signal-to-noise ratio over the GDA domain. Thick lines show the signal-to-noise ratio for trends beginning in AD 1900 in the GDA tree ring reconstructions (green), DAI (light blue) and CRU (dark blue) PDSI datasets. **c**, Time of emergence for model-predicted and observed PSDI signals in the GDA and in each individual regions, assuming a start in AD 2019. The thin horizontal line corresponds to the virtually certain level ($S/N > 2.57$, 99% confidence). Shading represents the maximum and minimum signal-to-noise ratios in the individual model simulations. Thick solid lines show the multi-model average signal-to-noise ratio in each region.

assuming a start in AD 1900, exceeds (and remains above) the reconstructed preindustrial variability[31]. Using the terminology used by the IPCC[32], a signal is 'likely' to be detectable when the signal-to-noise ratio exceeds 0.95 (66% confidence), 'very likely' to be detectable when the ratio exceeds 1.64 (that is, significant at 90% confidence), and 'virtually certain' to be detectable when the ratio exceeds 2.57 (99% confidence).

The mean model signal-to-noise ratio over the GDA domain (Fig. 3b) indicates three periods of interest in the twentieth and early twenty-first centuries. The signal increases throughout the first half of the twentieth century, becoming detectable at the likely level by AD 1950. However, models indicate that the signal should diminish between AD 1950 and AD 1975 and become undetectable even as the noise term becomes smaller with increasing record length. After AD 1975, the signal once again increases.

We find that the GDA (Fig. 3b) and two datasets[24,25,33] (see Methods) constructed from meteorological observations (Fig. 3b) show trends that are very similar to the multi-model mean. All three datasets indicate a detectable signal in the early twentieth century and a quick decrease mid-twentieth century. The two meteorological datasets indicate an increasing signal in recent decades (the drought atlases transition from tree-ring-derived reconstructions to their respective target datasets after 1975, we therefore exclude GDA data after that date; see Methods). Because we use pre-1850 drought atlas data to define the noise term, this detection analysis is largely independent of GCMs, except for the use of the models to generate the fingerprint.

The usefulness of the global approach is shown in Fig. 2c. Assuming a present-day (that is, 2019) start to minimize the effects of other historical forcings, the model-predicted signal in the GDA and in all

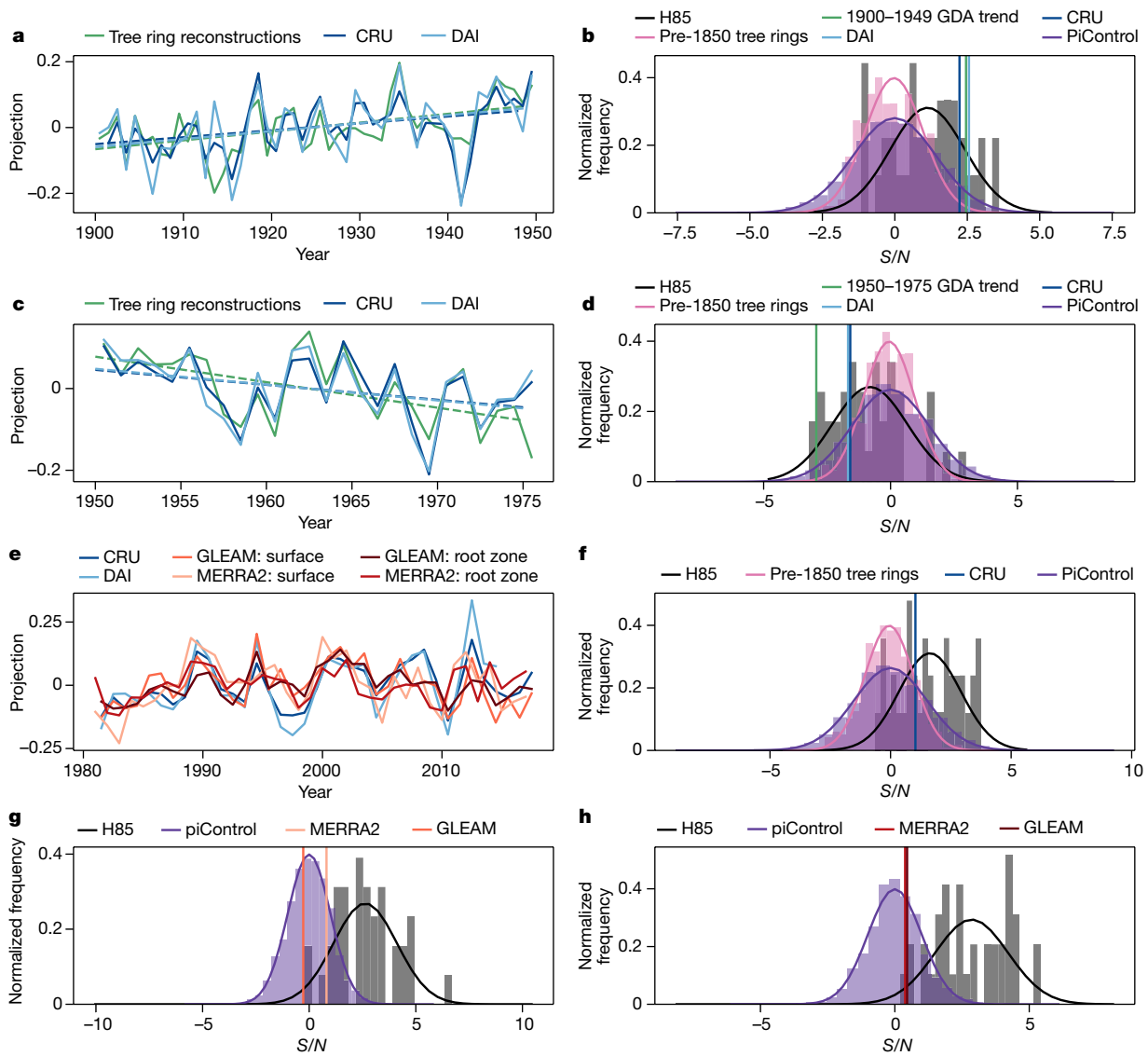

Fig. 4 | Detection and attribution results. a, Projection of 1900–1949 PDSI from the drought atlases and two instrumental datasets onto the fingerprint. **b**, Signal-to-noise ratios (*S*/*N*) in the three datasets (vertical lines), pre-1850 drought atlas projections (pink histogram), preindustrial control simulations (purple histogram) and H85 simulations (black histogram). All signals and distributions are normalized by dividing by the standard deviation of the drought atlas noise histogram. Solid lines show the best-fit Gaussian distribution for visual clarity. **c**, **d**, Analyses as in **a**, **b**, but for 1950–1975 trends. **e**, **f**, Analyses as in **a**, **b**, but for 1981–2017 trends. **e**, The projection of two surface and root-zone soil moisture datasets onto their respective fingerprints is also shown. **g**, Signal-to-noise ratios in the two surface soil moisture datasets (vertical lines), preindustrial control simulations (PiControl, purple histogram) and H85 simulations (black histogram). All signals and distributions are normalized by dividing by the standard deviation of the drought atlas noise histogram. **h**, Analysis as in **g**, but for root-zone soil moisture.

individual drought atlases monotonically increases under the greenhouse-gas-dominated RCP8.5 scenario. The average model projects a detectable signal in the GDA by 2036—earlier than in any of the individual drought atlas regions. Signal emergence is slowest in the MXDA (emerging by 2067) and ANZDA (emerging by 2073), owing to the small land areas and large internal variability of these regions. The NADA signal is also slow to emerge (by 2062) owing to large internal variability. Models project that the signal-to-noise ratios of the OWDA and MADA will cross the detectability threshold earlier: for OWDA (by 2049), mainly because the signal is strong, and for MADA (by 2047), because the noise term is comparatively small (Extended Data Fig. 1).

Detection and attribution

However, the signal in most drought atlases does not monotonically increase over the twentieth century. The principal components shown in Fig. 2d clearly indicate an increase from 1900 to 1949, a decrease from 1950 to 1975, and a subsequent increase; behaviour that is clearly apparent in the observationally based datasets (Fig. 3b).

To further compare models and observations, we perform a detection and attribution analysis over these three distinct time periods.

1900–1949

The projection of the GDA and the two meteorological datasets onto the PDSI fingerprint from Fig. 1a for 1900–1949 is shown in Fig. 4a. All three datasets increasingly resemble the fingerprint over this period, as illustrated by the positive trends in these fingerprint projections. The statistical significance of these signals can be assessed against total natural variability derived from the pre-1850 GDA. The trend for 1900–1949 is larger than all but one of the 50-year trends in the pre-1850 GDA projections: the signal (in all three datasets) is detectable at the very likely threshold. It is also compatible with 50-year trends in forced model simulations over the same period, thus indicating that a

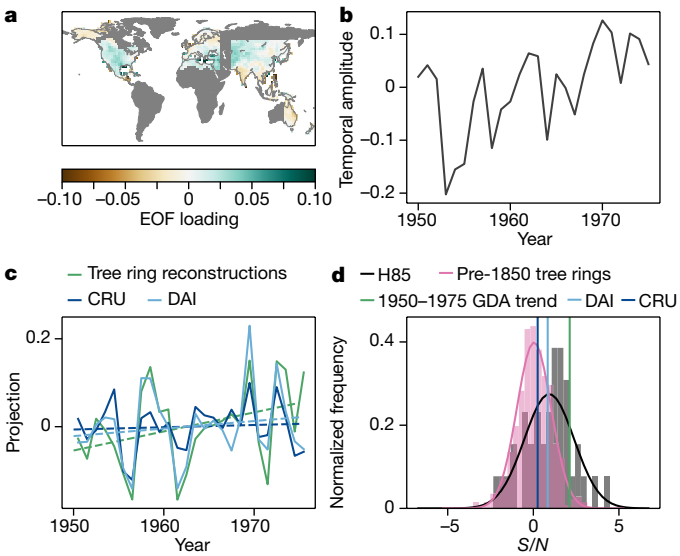

Fig. 5 | Aerosol attribution. a, The approximated aerosol fingerprint derived from historical CMIP5 simulations over 1950–1975. Note that this fingerprint explains less than 12% of the variance in the multi-model mean. **b**, The associated principal component, showing an increase over this time period. **c**, Projections of the GDA and two meteorological datasets onto this fingerprint. **d**, Formal detection and attribution analysis, as in Fig. 3d but with projections onto the approximated aerosol fingerprint shown in **a**.

detectable signature of external forcing is present in the first half of the twentieth century.

1950–1975

In contrast to the signal detected from 1900 to 1949, all three datasets are increasingly dissimilar to the fingerprint of 1950–1975 (Fig. 4c). This negative trend in the projection means that mid-century hydroclimate changes do not resemble the modelled response to the forcings (predominantly due to anthropogenic greenhouse gases) that determine the fingerprint (Fig. 2a). However, the 1950–1975 behaviour is also unusual in the context of preindustrial variability (Fig. 4d), while being compatible with the distribution of 26-year trends in forced models simulations over the same period. This suggests a possible role for external forcing, despite the increasing divergence from the expected fingerprint of greenhouse gas forcing.

Although greenhouse gases were important during the twentieth century, they were not the only forcing agents that shaped the climate. The mid-century period coincides with increasing anthropogenic aerosol forcing in the global mean[34,35], which has been shown to affect aspects of regional precipitation[36–38]. A formal attribution of these trends to anthropogenic aerosol emissions would require knowledge of the PDSI response to aerosol forcing. However, an aerosol fingerprint on global and regional hydroclimate remains unclear for several reasons: inter-model disagreement in the magnitude and sign of the forced response[39], uncertainties in aerosol forcing[40] and model representation (or lack thereof) of the indirect and direct aerosol effects and tropospheric cloud responses[39,41] (Methods and Extended Data Fig. 3). Here, we approximate an aerosol fingerprint by averaging PDSI from the H85 simulations over the restricted period 1950–1975 before calculating the leading EOF (Fig. 5a). We note that although anthropogenic aerosol forcing was increasing over this period, other forcings—particularly greenhouse gas emissions and the eruption of Mount Agung in 1963—also have a large role. Although the associated principal component displays a distinct upward trend (Fig. 5b), this EOF explains less than 12% of the variance in the multi-model mean over this period. Because internal variability is decreased by the averaging process, this low value reflects inter-model disagreement in the magnitude and sign of the forced response (Extended Data Fig. 3).

Nevertheless, this approximation of an aerosol fingerprint appears increasingly present in the GDA and meteorological datasets, although the signal is weak (Fig. 5c). Projecting pre-1850 tree ring reconstructions onto this approximate aerosol fingerprint and calculating the distribution of 26-year trends (Fig. 4b–f) yields a measure of noise, and suggests that the weak signal of the influence of aerosols is not detectable above natural variability (Fig. 5d). However, despite substantial ambiguity in the model-predicted response to aerosols, the H85 distribution of trends over this period is shifted to the right of the noise distribution, indicating that this fingerprint is increasingly present in the average H85 simulation. This is in contrast to the detection and attribution analysis shown in Fig. 4d, which suggests that the H85 simulations over this period are increasingly dissimilar to the greenhouse-gas-dominated fingerprint (Fig. 2a). Moreover, we note that the model-predicted signal is stronger in those models that include some representation of the indirect effects of aerosols, and that these models have generally been found[39,42] to be more reliable over this period (Extended Data Fig. 3).

Our results suggest a possible role for at least some non-greenhouse gas forcings during the mid-twentieth century, although further work is needed to rigorously identify the expected responses to individual forcings (particularly greenhouse gases, aerosols and volcanic eruptions) over this time period in order to robustly attribute the observed and modelled 1950–1975 trends.

1981 to present

Finally, at the end of the twentieth century, models indicate that the signal once again becomes positive. We choose to perform a formal detection and attribution analysis over the period 1981–2017 in order to incorporate two soil moisture datasets (MERRA-2[43], a reanalysis in which soil moisture is initialized with gauge-based precipitation observations, and GLEAM[16], a reanalysis constrained by satellite estimates of surface soil moisture, both of which begin in 1981). The projections of surface and root-zone soil moisture observations onto their respective fingerprints from Fig. 1b, c are consistent with the projections of the meteorological PDSI datasets onto the PDSI fingerprint (Fig. 4e). Positive trends in all of the projections indicate increasing similarity to the fingerprint and thus consistency with signals in the forced H85 models over the same period; however, they are not detectable at the likely level over background noise (Fig. 4f–h). Moreover, in the two soil moisture datasets the signal occurs in the left-hand tail of the distribution of forced model signals. This may be a signature of the recent 'hiatus'[44] in global surface warming, a period characterized by cool temperatures in the equatorial Pacific[45] and intensification of the trade winds[46]. Although the causes[47], relevance[48] and even statistical existence[49] of the hiatus are debatable, our finding is consistent with literature that has identified differences in the multi-model mean and observations across multiple variables[46,50]. Alternatively, the relatively weak signal may reveal a more serious disagreement between the model and observations. However, if the end of hiatus conditions brings models and observations into closer agreement, then we should expect a detectable signal by the middle of the twenty-first century (by 2054, assuming a start in 1981), when even the most conservative model projects emergence at a virtually certain level.

Noise from model simulations

Suppose we had not used drought atlases to estimate noise, but instead followed the traditional route of using preindustrial control simulations. Traditional noise estimates from these simulations estimate larger natural variability than the GDA, despite excluding—by design—the responses to natural forcings that could increase that variability (Fig. 4b–f). The discrepancy may also arise from the brevity of the tree ring record compared to concatenated model noise: the 450 years in the GDA may fail to capture the full range of variability. However, sensitivity tests using different periods and regions do not indicate any systematic bias in noise estimates (Methods, Extended Data Fig. 4 and Supplementary Table 1). These results indicate that noise estimates

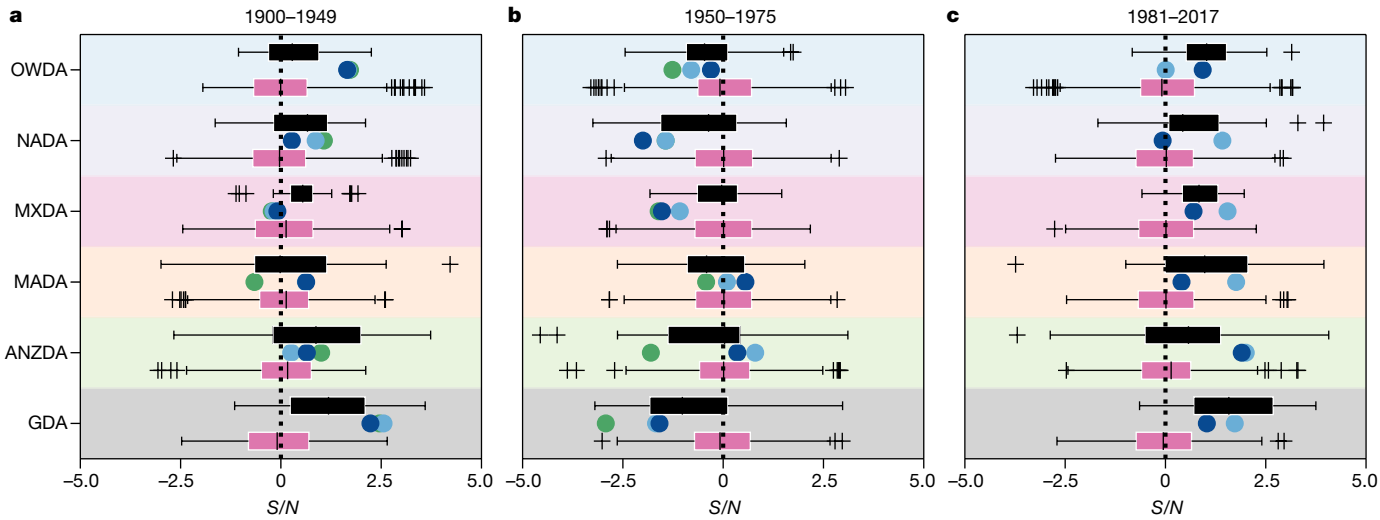

Fig. 6 | Regional detection and attribution. a–c, Signal-to-noise ratios in individual drought atlas regions and the GDA for 1900–1049 (**a**), 1950–1975 (**b**) and 1981–2017 (**c**). For all model and observational data, the signal is defined relative to the H85 fingerprint in Figs. 1a–e, 2a. The black box plots represent the *S*/*N* ratios in H85 simulations; the pink box plots the *S*/*N* ratio distributions from preindustrial noise (estimated from pre-1850 drought atlas data). For all box plots, the box extends from the lower to upper quartile values of the data, with a line at the median and the whiskers represent the interquartile range multiplied by 1.5; values outside this range are plotted as outliers (+). *S*/*N* ratios from the drought atlases over the three periods are plotted as green dots in **a** and **b**, *S*/*N* ratios from the CRU (dark blue) and DAI (light blue) datasets are plotted as dots in **a–c**.

from model-derived preindustrial control simulations provide more conservative detection estimates. Despite this fact, the signal for 1900–1949, for instance, remains detectable at the virtually certain level.

Regional detection and attribution

Repeating the analysis in individual drought atlas regions confirms the usefulness of the global approach for signal detection. The signal-to-noise ratios in each individual drought atlas are shown in Fig. 6. All signals and noise are defined by projection onto the greenhouse-gas-dominated fingerprints shown in Fig. 1a–e (regional) and 2a (global).

We find no detectable signal in any individual region, because of the large internal variability and reduced signal strength. However, certain trends are notable: with the exception of MXDA and MADA, for which the trend is ambiguous, trends in the early half of the twentieth century are positive everywhere. Negative signals are present in the OWDA, NADA and MXDA in both models and observations at mid-twentieth century. In the recent period, trends are positive almost everywhere and are compatible with forced distributions in all regions.

Our results suggest that anthropogenic influences on global hydroclimate were present throughout the twentieth century, albeit in different forms. The influence of greenhouse gases is clearly visible in the early half of the century, but their effect was likely counteracted by increased anthropogenic aerosol emissions by mid-twentieth century. Future research is needed to more precisely understand the impacts of different forcing agents—and particularly aerosols and greenhouse gases—on global and regional hydroclimate and to extend the palaeoclimate reconstructions into different regions. However, models project and observations show a re-emerging greenhouse gas signal towards the end of the twentieth century, and this signal is likely to grow stronger in the next several decades. The human consequences of this, particularly drying over large parts of North America and Eurasia, are likely to be severe.

Online content

Any methods, additional references, Nature Research reporting summaries, source data, statements of data availability and associated accession codes are available at https://doi.org/10.1038/s41586-019-1149-8.

Received: 30 October 2018; Accepted: 4 March 2019;
Published online 1 May 2019.

1. Cook, E. R., Seager, R., Cane, M. A. & Stahle, D. W. North American drought: reconstructions, causes, and consequences. *Earth Sci. Rev.* **81**, 93–134 (2007).
2. Cook, E. R. et al. Megadroughts in North America: placing IPCC projections of hydroclimatic change in a long-term palaeoclimate context. *J. Quaternary Sci.* **25**, 48–61 (2010).
3. Cook, E. R. et al. Old World megadroughts and pluvials during the Common Era. *Sci. Adv.* **1**, e1500561 (2015).
4. Stahle, D. W. et al. The Mexican drought atlas: tree-ring reconstructions of the soil moisture balance during the late pre-Hispanic, colonial, and modern eras. *Quat. Sci. Rev.* **149**, 34–60 (2016).
5. Cook, E. R. et al. Asian monsoon failure and megadrought during the last millennium. *Science* **328**, 486–489 (2010).
6. Palmer, J. G. et al. Drought variability in the eastern Australia and New Zealand summer drought atlas (ANZDA, ce 1500–2012) modulated by the interdecadal pacific oscillation. *Environ. Res. Lett.* **10**, 124002 (2015).
7. Cook, B. I., Anchukaitis, K. J., Touchan, R., Meko, D. M. & Cook, E. R. Spatiotemporal drought variability in the Mediterranean over the last 900 years. *J. Geophys. Res.* **121**, 2060–2074 (2016).
8. Griffin, D. & Anchukaitis, K. J. How unusual is the 2012–2014 California drought? *Geophys. Res. Lett.* **41**, 9017–9023 (2014).
9. Cook, B. I., Seager, R. & Smerdon, J. E. The worst North American drought year of the last millennium: 1934. *Geophys. Res. Lett.* **41**, 7298–7305 (2014).
10. Bindoff, N. et al. *Detection and Attribution of Climate Change: from Global to Regional* Vol. 10, 867–952 (Cambridge Univ. Press, Cambridge, 2013).
11. Berg, A. & Sheffield, J. Climate change and drought: the soil moisture perspective. *Curr. Clim. Change Rep.* **4**, 180–191 (2018).
12. Bonfils, C. et al. Competing influences of anthropogenic warming, ENSO, and plant physiology on future terrestrial aridity. *J. Clim.* **30**, 6883–6904 (2017).
13. Milly, P. C. & Dunne, K. A. Potential evapotranspiration and continental drying. *Nat. Clim. Change* **6**, 946–949 (2016).
14. Swann, A. L., Hoffman, F. M., Koven, C. D. & Randerson, J. T. Plant responses to increasing CO_2 reduce estimates of climate impacts on drought severity. *Proc. Natl Acad. Sci. USA* **113**, 10019–10024 (2016).
15. Taylor, K. E., Stouffer, R. J. & Meehl, G. A. An overview of CMIP5 and the experiment design. *Bull. Am. Meteorol. Soc.* **93**, 485–498 (2012).
16. Martens, B. et al. GLEAM v3: satellite-based land evaporation and root-zone soil moisture. *Geosci. Model Dev.* **10**, 1903–1925 (2017).
17. Reichle, R. H. et al. Assessment of MERRA-2 land surface hydrology estimates. *J. Clim.* **30**, 2937–2960 (2017).
18. Santer, B. et al. Separating signal and noise in atmospheric temperature changes: the importance of timescale. *J. Geophys. Res.* **116**, D22105 (2011).
19. Santer, B. D. et al. Ocean variability and its influence on the detectability of greenhouse warming signals. *J. Geophys. Res.* **100**, 10693–10725 (1995).
20. Santer, B. D. et al. Identifying human influences on atmospheric temperature. *Proc. Natl Acad. Sci. USA* **110**, 26–33 (2013).
21. Marvel, K. & Bonfils, C. Identifying external influences on global precipitation. *Proc. Natl Acad. Sci. USA* **110**, 19301–19306 (2013).
22. van Vuuren, D. P. et al. The representative concentration pathways: an overview. *Clim. Change* **109**, 5–31 (2011).
23. Cook, B. I., Smerdon, J. E., Seager, R. & Coats, S. Global warming and 21st century drying. *Clim. Dyn.* **43**, 2607–2627 (2014).

24. Dai, A. Characteristics and trends in various forms of the Palmer drought severity index during 1900–2008. *J. Geophys. Res.* **116**, D12115 (2011).
25. van der Schrier, G., Briffa, K., Jones, P. & Osborn, T. Summer moisture variability across Europe. *J. Clim.* **19**, 2818–2834 (2006).
26. Stott, P. A. & Tett, S. F. Scale-dependent detection of climate change. *J. Clim.* **11**, 3282–3294 (1998).
27. Marvel, K. et al. External influences on modeled and observed cloud trends. *J. Clim.* **28**, 4820–4840 (2015).
28. Baek, S. H. et al. Precipitation, temperature, and teleconnection signals across the combined North American, monsoon Asia, and Old World drought atlases. *J. Clim.* **30**, 7141–7155 (2017).
29. Santer, B. D. et al. Identification of human-induced changes in atmospheric moisture content. *Proc. Natl Acad. Sci. USA* **104**, 15248–15253 (2007).
30. Santer, B. D. et al. Human and natural influences on the changing thermal structure of the atmosphere. *Proc. Natl Acad. Sci. USA* **110**, 17235–17240 (2013).
31. Hegerl, G. C. et al. *Good Practice Guidance Paper on Detection and Attribution Related to Anthropogenic Climate Change* (IPCC, 2010).
32. Mastrandrea, M. D. et al. *Guidance Note for Lead Authors of the IPCC Fifth Assessment Report on Consistent Treatment of Uncertainties* (IPCC, 2010).
33. Dai, A. & Zhao, T. Uncertainties in historical changes and future projections of drought. Part I: estimates of historical drought changes. *Clim. Change* **144**, 519–533 (2017).
34. Skeie, R. et al. Anthropogenic radiative forcing time series from pre-industrial times until 2010. *Atmos. Chem. Phys.* **11**, 11827–11857 (2011).
35. Miller, R. L. et al. CMIP5 historical simulations (1850–2012) with GISS ModelE2. *J. Adv. Model. Earth Syst.* **6**, 441–478 (2014).
36. Biasutti, M. & Giannini, A. Robust Sahel drying in response to late 20th century forcings. *Geophys. Res. Lett.* **33**, L11706 (2006).
37. Polson, D., Bollasina, M., Hegerl, G. & Wilcox, L. Decreased monsoon precipitation in the Northern Hemisphere due to anthropogenic aerosols. *Geophys. Res. Lett.* **41**, 6023–6029 (2014).
38. Bollasina, M. A., Ming, Y. & Ramaswamy, V. Anthropogenic aerosols and the weakening of the South Asian summer monsoon. *Science* **334**, 502–505 (2011).
39. Wilcox, L. J., Highwood, E. J. & Dunstone, N. J. The influence of anthropogenic aerosol on multi-decadal variations of historical global climate. *Environ. Res. Lett.* **8**, 024033 (2013).
40. Pincus, R., Forster, P. M. & Stevens, B. The radiative forcing model intercomparison project (RFMIP): experimental protocol for CMIP6. *Geosci. Model Dev.* **9**, 3447–3460 (2016).
41. Zelinka, M. D., Andrews, T., Forster, P. M. & Taylor, K. E. Quantifying components of aerosol–cloud–radiation interactions in climate models. *J. Geophys. Res.* **119**, 7599–7615 (2014).
42. Ekman, A. M. Do sophisticated parameterizations of aerosol-cloud interactions in CMIP5 models improve the representation of recent observed temperature trends? *J. Geophys. Res.* **119**, 817–832 (2014).
43. Gelaro, R. et al. The modern-era retrospective analysis for research and applications, version 2 (MERRA-2). *J. Clim.* **30**, 5419–5454 (2017).
44. Medhaug, I., Stolpe, M. B., Fischer, E. M. & Knutti, R. Reconciling controversies about the 'global warming hiatus'. *Nature* **545**, 41–47 (2017).
45. Kosaka, Y. & Xie, S.-P. Recent global-warming hiatus tied to equatorial Pacific surface cooling. *Nature* **501**, 403–407 (2013).
46. England, M. H. et al. Recent intensification of wind-driven circulation in the Pacific and the ongoing warming hiatus. *Nat. Clim. Change* **4**, 222–227 (2014).
47. Schmidt, G. A., Shindell, D. T. & Tsigaridis, K. Reconciling warming trends. *Nat. Geosci.* **7**, 158–160 (2014).
48. Johansson, D. J. A., O'Neill, B. C., Tebaldi, C. & Häggström, O. Equilibrium climate sensitivity in light of observations over the warming hiatus. *Nat. Clim. Change* **5**, 449–453 (2015).
49. Risbey, J. S. et al. A fluctuation in surface temperature in historical context: reassessment and retrospective on the evidence. *Environ. Res. Lett.* **13**, 123008 (2018).
50. Trenberth, K. E., Fasullo, J. T., Branstator, G. & Phillips, A. S. Seasonal aspects of the recent pause in surface warming. *Nat. Clim. Change* **4**, 911–916 (2014).

Acknowledgements We acknowledge the World Climate Research Programme's Working Group on Coupled Modelling, which is responsible for CMIP, and we thank the climate modelling groups (listed in Supplementary Table 3) for producing and making available their model output. For CMIP, the US Department of Energy's Program for Climate Model Diagnosis and Intercomparison provided coordinating support and led development of the software infrastructure in partnership with the Global Organization for Earth System Science Portals. We thank K. Taylor, G. Schmidt and R. Pincus for discussions. K.M. and C.J.W.B. were supported by the US Department of Energy Biological and Environmental Research Grant DE-SC0014423. K.M., B.I.C. and A.P.W. were supported for this work by the NASA Modeling, Analysis, and Prediction program (NASA 80NSSC17K0265). J.E.S. was supported in part by US National Science Foundation (NSF) grants AGS-1243204 and AGS-1602581; J.E.S. and A.P.W. were further supported by NSF grant OISE-1743738 and A.P.W. was supported by NSF grant AGS-1703029. P.J.D. was supported through PCDMI SFA funding from the DOE Regional and Global Model Analysis Program. Work at LLNL was performed under the auspices of the US Department of Energy under contract DE-AC52-07NA27344.

Reviewer information *Nature* thanks Hans Linderholm and the other anonymous reviewer(s) for their contribution to the peer review of this work.

Author contributions K.M. and B.I.C. designed the study. K.M. performed the analyses with contributions from B.I.C. C.J.W.B. contributed to developing and applying the detection and attribution methodology. A.P.W. provided the code to calculate PSDI from CMIP5 model data. J.E.S. and A.P.W provided guidance on interpretation of the drought atlas data. P.J.D. provided the code to download and access CMIP5 data. K.M. and B.I.C. wrote the manuscript with contributions from all authors.

Competing interests The authors declare no competing interests.

Additional information

Extended data is available for this paper at https://doi.org/10.1038/s41586-019-1149-8.
Supplementary information is available for this paper at https://doi.org/10.1038/s41586-019-1149-8.
Reprints and permissions information is available at http://www.nature.com/reprints.
Correspondence and requests for materials should be addressed to K.M.
Publisher's note: Springer Nature remains neutral with regard to jurisdictional claims in published maps and institutional affiliations.

© The Author(s), under exclusive licence to Springer Nature Limited 2019

METHODS

PDSI. The PDSI[51] is a soil-moisture-based drought indicator, representing variability in soil moisture using a two-layer bucket model[52,53] that integrates changes in moisture supply (precipitation) and demand (evapotranspiration) over timescales of about 12 months. PDSI is a standardized index, in which values of zero represent baseline average conditions and positive or negative values indicating wet or dry departures from the baseline climatology. In this study, we track reconstructed, observed and simulated PDSIs, because PDSI is the target variable for existing drought atlases.

PDSI is a drought index that is widely used for observational analyses[54], as a target for palaeoclimate reconstructions[1] and in model simulations of the past and future[22,23]. Previous analyses have demonstrated that results from PDSI compare favourably with surface soil moisture simulated by more sophisticated land-surface and hydrologic models that are based on physical measurements[23,55]. Differences may arise between PDSI and total soil moisture in the future, when the influence of atmospheric CO_2 on plant physiology is taken into account[12] and this metric has received important (and valid) criticism regarding its utility for both drought monitoring and in climate change projections of drought risk[11,12,14]. General criticisms are twofold: (1) the offline nature of the calculation of PDSI and (2) the simplification or omission of important processes, such as snow or the physiological impact of CO_2 on plant water use efficiency and evapotranspiration. Because of its offline nature (in which climate data drives the model, but feedback effects from the land to the atmosphere are disabled), there are concerns that the PDSI may overestimate the impact of rising temperatures on drought by effectively counting the temperature impact twice[56,57]. For example, during droughts the surface dries out and plants close their stomata, reducing latent heat fluxes. This causes increased sensible heating, which increases air temperatures. However, this warming is a clear response to the drought, and if these temperatures are used to force an offline land-surface model, they will have a disproportionate impact on the drought. This is a critique that may be applied to any offline land-surface model, and the degree to which this issue exacerbates temperature impacts on regional droughts is still debated. Similarly, the physiological response of plants to rising atmospheric CO_2 may increase the plant water use efficiency and preserve soil moisture in the root zone. Neglecting this CO_2–physiology feedback in the offline calculation of potential evapotranspiration (by keeping the stomatal resistance constant in the computation of the potential evapotranspiration) may overpredict future drying trends from warming in PDSI[12,14]. However, the net impact of this physiological effect depends on how aridity is defined[12].

Despite these critiques, there is generally broad agreement between some estimates of surface soil moisture variability and trends calculated from PDSI and more sophisticated models of land surface hydrology. For example, when forced with the same meteorological input data, summer soil moisture over the Sierra Nevada Mountains estimated from PDSI and the state-of-the-art variable infiltration capacity model[55] correlate with $r = 0.93$. Similarly, PDSI and soil moisture taken from coupled climate models also show good agreement regarding the intensity and spatial extent of drying and wetting trends in model projections[23,58,59] of greenhouse gas forcing in the twenty-first century. It was previously shown that aridity trends in the twenty-first century with potential evapotranspiration (PET)-derived PDSI were in good agreement with near-surface soil moisture trends, although disparities were identified when compared with deeper soil moisture trends[12]. The divergence between near-surface and deep soil moisture within the coupled models is nevertheless as large as or larger than the difference between PDSI and model soil moisture[23].

We show that the surface area over which drying is predicted by the models tends to be larger with PDSI and the surface soil moisture (70% and 76% of the GDA land surface, respectively) than with the root zone soil moisture (59%; Fig. 2a–c). This result is consistent with recent model results[12] that show that the area of land that is permanently arid in the future appears to be much larger when aridity indices that are dominated by the behaviour of meteorological variables (such as PDSI and the soil moisture in surface layers that interact closely with the atmosphere) are used than with plant-based aridity indices (such as the root zone soil moisture). This is mainly owing to a modelled plant physiology feedback in which plant evapotranspiration is reduced, preserving soil moisture in the root zone. We also note that the PDSI fingerprints differs from the soil moisture fingerprints in Alaska and northeast Asia, probably because PSDI does not include data on permafrost and soil freezing, and treats all precipitation as rain. Nevertheless, the PDSI and surface soil moisture fingerprints have the same sign in 76% of the GDA land area, while PDSI and root zone soil moisture fingerprints have the same sign in over 65% of the area. Surface and root zone fingerprints have the same sign in over 81% of the GDA land area.

Reconstructions. The three drought atlases (NADA, MXDA and OWDA) that were used in this study are available from the Tree-Ring Drought Atlas Portal at http://drought.memphis.edu.

The most recently updated versions of ANZDA (https://www.dropbox.com/s/nrizk1a1a289awh/anzdaV2.nc) and MADA (https://www.dropbox.com/s/n2lo99h9qn17prg/madaV2.nc) that are used in this analysis are available from the indicated websites.

To construct GDA, all atlases were downloaded and regridded to a common 2.5° latitude–longitude grid using the CDAT 'regrid2' tool, which uses an interpolation that preserves the area-weighted mean. In areas in which there is overlap, data from the MXDA supersedes that from the NADA, because MXDA includes more proxies over the domain (and has been shown to be more skilful over the reconstructed domain) than what is available in the NADA[4]. The GDA begins in the year AD 1400, when data from MXDA and ANZDA become available. A uniform mask is imposed at every time step: if a grid cell is missing data for any year between 1400 and 2005, it is masked for all times in the record. Following this masking process, we have comprehensive data for 54% of the non-Antarctic global land area.

The drought atlases consist of tree ring reconstructions until the 1970s, after which they switch over the target instrumental dataset, which is different for each drought atlas. Spatially averaged time series (or principal components) may exhibit discontinuities at the time at which a drought atlas switches from tree rings to instrumental data. This is because the instrumental data generally have a much higher spatial variance than the tree rings, so variability and trends in the instrumental period are muted relative to the tree ring period. For this reason, tree-ring-based time series used in the main text were only used up until the end of 1975, when the ANZDA drought atlas (the first to do so) switched to instrumental data.

Meteorological datasets. We used two datasets that were derived from recent observations. In the first dataset[25], PDSI was calculated from instrumental temperature and precipitation that was taken from version 3.21 of the University of East Anglia CRU climate grids and PET was calculated using the Penman–Monteith formula. These are gridded monthly mean values, interpolated over land from individual station observations to a spatially uniform half-degree grid. The data that we used are available at https://crudata.uea.ac.uk/cru/data/drought/.

We regridded this dataset to the same common grid as the models and calculated the average over the summer season. The second observational dataset that we used was described previously[60], consisting of monthly PDSI over global land areas on a 2.5° grid that was computed using observed monthly surface air temperature and precipitation data from the National Center for Environmental Prediction (NCEP) reanalysis. We calculated means over the summer season from these monthly values. Two PDSI datasets were generated previously using the Thornthwaite and Penman–Monteith formulations of potential evapotranspiration. Here we only used the Penman–Monteith version, which is available at https://rda.ucar.edu/datasets/ds299.0/.

PDSI calculations from simulations. The PDSI is calculated as described previously[23] for two sets of simulations archived by the CMIP5[15]: preindustrial control and historical simulations extended post-2005 with RCP8.5 simulations (H85). For H85 simulations, we calculate model PDSIs for 1850–2099 using the Penman–Monteith formulation of potential evapotranspiration. We use 1921–2000 as the baseline period for PDSI in the H85 simulations. For PDSI calculations in each individual preindustrial control simulation, we use the full time interval of simulation as the baseline period. The PDSI index is computed monthly, but all analyses are based on PDSI averaged for the summer season: June–July–August for the Northern Hemisphere and December–January–February for the Southern Hemisphere. The mask determined from the GDA is applied to all model results throughout all analyses.

Simulated soil moisture. In accordance with a previous publication[23], we also calculate standardized soil moisture metrics from the GCMs by integrating total soil moisture for June–July–August (December–January–February in the Southern Hemisphere) from the surface to 30 cm (surface) and from the surface to 2–3 m (root zone). We use the CMIP5 'mrlsl' variable, defined as the mass of water in each soil layer (all phases). These are standardized at each grid cell such that the soil moisture metrics have the same mean and temporal s.d. as the model PDSI during the 1921–2000 interval at each grid cell. This enables direct comparisons between variability and trends in shallow and deep soil moisture while independently preserving any low-frequency variability or trends in the model soil moisture that is distinct from the PDSI calculation. This standardization does not impose any artificial constraints that would force the three metrics to agree in terms of variability or future trends, allowing soil moisture at the surface and in the root zone to be used as indicators of drought in a manner that is largely independent of PDSI. Supplementary Table 2 contains information about the number of soil layers and approximate depths used for the calculation of soil moisture indices at the surface and in the root zone.

Observation-based soil moisture datasets. For recent decades, we also evaluated two observation-based datasets that provided estimates of both surface and root-zone soil moisture at the global scale. The first is MERRA-2, a global reanalysis product available from 1981 to 2017[43] that assimilates a variety of surface and

satellite datasets. In MERRA-2, all surface hydrologic variables (including soil moisture) are prognostically calculated using observation-based precipitation and other variables provided by the reanalysis (for example, temperature)[17]. Broadly, soil moisture estimates from MERRA-2 generally agree well with in situ soil moisture measurements[17]. The second dataset that we used is GLEAM version 3.2a, a land-surface reanalysis that provides estimates of terrestrial evapotranspiration and soil moisture (surface and root zone) using a land-surface model forced by atmospheric input data and constrained by satellite estimates of vegetation stress, snow cover and soil moisture[16]. In contrast to other reanalyses, including MERRA-2, GLEAM directly assimilates satellite-based soil moisture estimates into the top layer of the soil model, providing additional observational constraints on both evapotranspiration, and surface and root-zone soil moisture. As with MERRA-2, GLEAM has been extensively evaluated against in situ measurements of soil moisture and evapotranspiration[16]. For comparisons with the climate model simulations, surface and root-zone soil moisture from MERRA-2 and GLEAM were standardized to the same mean and variance as the GCM surface and root-zone soil moisture.

Detection and attribution toolkit. *Fingerprint.* There are three components in a detection and attribution study. The fingerprint $F(\theta, \phi)$ of climate change is the spatial pattern, generally a function of latitude θ and longitude ϕ, that characterizes the climate system response to external forcing[18–21]. In much of the literature (for example, refs. [19,61] and the references therein), the fingerprint is defined as the leading EOF of the spatiotemporal covariance matrix that results from first averaging over members of each CMIP5 historical model ensemble and then over models. This ensures that the average is not dominated by models that submitted many historical ensemble members to CMIP5. Because internal variability is uncorrelated across models and ensemble members, the leading EOF should reflect a common response to the particular collection of forcing data that are present in the historical simulations. These generally include natural forcing data (volcanic eruptions and solar variations) as well as anthropogenic ozone depletion, land-use change, aerosols and greenhouse gases. The fingerprint $F(\theta, \phi)$ summarizes our best understanding of how the variable in question responds to external forcing. We note the similarity between the leading EOF (Fig. 2a) and the linear trend pattern (Extended Data Fig. 2), an agreement characterized by a pattern correlation that exceeds 99%. Because RCP8.5 is dominated by greenhouse gas emissions, they are the primary contributor to the fingerprints shown in Fig. 1. Repeating the analysis with the fingerprint generated from years 2006–2099 of RCP8.5 only (data not shown) does not change the conclusions.

Because CMIP5 historical simulations end in 2005, we extend them to 2099 by splicing with the corresponding RCP8.5 simulation (H85). For each H85 simulation, year t and grid cell (θ, ϕ), we calculate the summer season (June–July–August in the Northern Hemisphere, December–January–February in the southern) average PDSI as described previously[23]. We then average over all ensemble members of a particular model, and then over all models, to obtain multi-model mean PDSI time series. The averaging process decreases internal variability—which is expected to be uncorrelated across different models and realizations—and reveals the forced response. The fingerprint is defined as the leading empirical orthogonal function of the 1860–2099 multi-model mean PDSI, weighted by the grid-cell area. We also calculate fingerprints for surface (30 cm) and root zone (2 m) soil moisture over 1900–2099 using the same method.

Approximate aerosol fingerprints are also calculated as described in the main text. Aerosol emissions[62], forcing[40], fast cloud adjustments[41] and responses[39] are highly uncertain across models. This is shown in Extended Data Fig. 3, where the approximated aerosol fingerprint has been calculated from two groups of models over the period 1950–1975: those with a representation of the indirect effect of sulfate aerosols and those without (see table 1 of a previously published study[39] for a list of such models). The principal component that was associated with the EOF calculated from models that included the indirect effects showed upward trends, whereas the principal component that was associated with models that excluded these effects showed no trend. Moreover, the spatial fingerprints associated with these two groups of models differ. The fingerprint calculated from models that include indirect effects shows moistening over the United States and much of Europe and the Levant, and drying in Australia as shown for the aerosol fingerprint in Fig. 5. The fingerprint calculated from models without indirect effects shows drying over much of the southwestern United States and no large changes in Australia. We urge caution with the interpretation of these fingerprints, however, as they explain less than 11% of the variance in their respective multi-model means.

Signal. Given a dataset of observed, reconstructed or simulated values $\mathcal{O}(\theta, \phi, t)$, the projection $P(t)$ onto the fingerprint $F(\theta, \phi)$ is given by $P(t) = \sum_{\theta,\phi} \mathcal{O}(\theta, \phi, t)F(\theta, \phi)w(\theta, \phi)$ where $w(\theta,\phi)$ is the grid cell area. Physically, this measures the spatial covariance between the searched-for fingerprint and the observational or model data as a function of time. If the fingerprint is increasingly present in the data, then $P(t)$ should show an upward trend. As previously described[18], we define the signal $S(L)$ as the L-length trend in $P(t)$, obtained by least-squares regression. This process reduces multidimensional observations, which vary across space and time, to a single scalar signal.

Noise. In order to assess the significance of a signal, we need an understanding of how internal climate variability might project onto the fingerprint. We do this in two ways: first, we project drought atlas-derived PDSI values onto the model-derived fingerprint, as in Fig. 2a, and take pre-1850 values to represent preindustrial noise that results from internal or naturally forced variability. Second, we calculate PDSI, surface soil moisture and root-zone soil moisture for the CMIP5 preindustrial control simulations. By concatenating each preindustrial control simulation for each variable and projecting the result onto the relevant fingerprint (Fig. 1a–c), we obtain a long (4,673 years) projection time series. For a signal of length L years, we calculate all possible L-length trends in this projection time series. The standard deviation of this distribution, denoted $N(L)$ provides a measure of noise in the trends: the likelihood of observing a given signal purely due to natural variability. Unless otherwise specified, PDSI noise is defined using the tree-ring-based method. Because there are no direct pre-1850 reconstructions of soil moisture, noise for surface and root-zone soil moisture is always defined using model preindustrial control simulations.

We find no systematic differences in 30- or 50-year noise terms estimated from years that were early (1400–1600) and late (1650–1850) in the preindustrial record (Extended Data Fig. 4). Moreover, Supplementary Table 1 indicates that our results are not highly sensitive to calculating noise dating from AD 1100, rather than AD 1400.

We have no recent observations of unforced variability to assess variability in soil moisture, and therefore rely on the credibility of GCMs to simulate this. We note that there is substantial uncertainty in observed soil moisture, and as pointed out previously[54], uncertainties in global precipitation measurements are large sources of this uncertainty.

Signal-to-noise ratio. We then compute the dimensionless signal-to-noise ratio $(S(L)/N(L))$ for a predetermined period of L years. We use the two-tailed z-test throughout to provide a conservative estimate of significance. If the dimensionless signal-to-noise ratio exceeds 0.95, 1.64 or 2.57, the L-length signal is considered detectable at 66%, 90% or 99% confidence, respectively (defined by IPCC guidelines as likely, very likely or virtually certain), relative to our best current multi-model estimates of natural internal variability[10]. Similarly, we compute $S(L)/H(L)$ where H is the projections of PDSI, surface soil moisture and root-zone soil moisture from the H85 climate simulations onto the fingerprint $F(\theta, \phi)$. If the signal-to-noise ratio lies within the 5–95% confidence interval obtained from CMIP5 H85 simulations, the signal is considered compatible with the combination of external forcing data present in those simulations. If an observed signal is both detectable and compatible with the CMIP5 forced distribution, it is considered attributable to that particular combination of external forcing analyses. However, an observed signal can be compatible with external forcing but too weak to emerge from the background of internal variability; or it can be detectable but not compatible with external forcing (if it is incompatible with both unforced and forced model distributions). The latter case is cause for concern and results from some combination of the following: model failure to realistically capture the forced sign and amplitude of the response, uncertainties in the forcing data themselves, model underestimation of internal variability or observational uncertainties.

Sensitivity tests. In the main text, we report a detectable trend in 1900–1949 PDSI in the GDA. The GDA, however, is the combination of data from five different drought atlases. We therefore repeat the exercise for each individual drought atlas, calculating fingerprints, noise and the signal for each region. The resulting 1900–1949 signal-to-noise ratios are shown in Supplementary Table 3. We also perform calculations for two other composite drought atlases: one in which NADA has been removed (because the target dataset for the NADA is different than for the other drought atlases, and because there were large droughts in the 1930s) and one in which we combine OWDA, NADA and MADA only, in order to obtain a noise time series that extends back to AD 1100. We note that the signal is significant at the likely level only in the OWDA, but combining the different drought atlases yields a larger signal-to-noise ratio that is robust to excluding the NADA and extending noise back to AD 1100.

Data availability

All model data used in this paper are available through the Earth System Grid (see https://esgf-node.llnl.gov/projects/esgf-llnl/) and freely available for download. All observational and reconstructed PDSI and soil moisture data are freely available for download from the indicated links. Data for NADA, MXDA, OWDA, http://drought.memphis.edu; ANZDA, https://www.dropbox.com/s/nrizk1a1a289awh/anzdaV2.nc; MADA, https://www.dropbox.com/s/n2lo99h9qn17prg/madaV2.nc; CRU, https://crudata.uea.ac.uk/cru/data/drought/; DAI, https://rda.ucar.edu/datasets/ds299.0/; MERRA-2, https://goldsmr4.gesdisc.eosdis.nasa.gov/data/MERRA2_MONTHLY/; GLEAM, https://www.gleam.eu.

Code availability

Analysis code written in Python is available at GitHub (https://github.com/kate-marvel/drought-atlas).

51. Palmer, W. C. *Meteorological Drought*. Research Paper No. 45 (US Department of Commerce, 1965).
52. Guttman, N. B. Comparing the Palmer drought index and the standardized precipitation index. *J. Am. Water Resour. Assoc.* **34**, 113–121 (1998).
53. Vicente-Serrano, S. M., Beguería, S. & López-Moreno, J. I. A multiscalar drought index sensitive to global warming: the standardized precipitation evapotranspiration index. *J. Clim.* **23**, 1696–1718 (2010).
54. Trenberth, K. E. et al. Global warming and changes in drought. *Nat. Clim. Change* **4**, 17–22 (2014).
55. Williams, A. P. et al. Contribution of anthropogenic warming to California drought during 2012–2014. *Geophys. Res. Lett.* **42**, 6819–6828 (2015).
56. Seneviratne, S. I. et al. Investigating soil moisture–climate interactions in a changing climate: a review. *Earth Sci. Rev.* **99**, 125–161 (2010).
57. Yin, D., Roderick, M. L., Leech, G., Sun, F. & Huang, Y. The contribution of reduction in evaporative cooling to higher surface air temperatures during drought. *Geophys. Res. Lett.* **41**, 7891–7897 (2014).
58. Dai, A. Increasing drought under global warming in observations and models. *Nat. Clim. Change* **3**, 52–58 (2013).
59. Feng, S., Trnka, M., Hayes, M. & Zhang, Y. Why do different drought indices show distinct future drought risk outcomes in the US great plains? *J. Clim.* **30**, 265–278 (2017).
60. Dai, A., Trenberth, K. E. & Qian, T. A global dataset of Palmer drought severity index for 1870–2002: relationship with soil moisture and effects of surface warming. *J. Hydrometeorol.* **5**, 1117–1130 (2004).
61. Hasselmann, K. Optimal fingerprints for the detection of time-dependent climate change. *J. Clim.* **6**, 1957–1971 (1993).
62. Smith, S. J. et al. Anthropogenic sulfur dioxide emissions: 1850–2005. *Atmos. Chem. Phys.* **11**, 1101–1116 (2011).

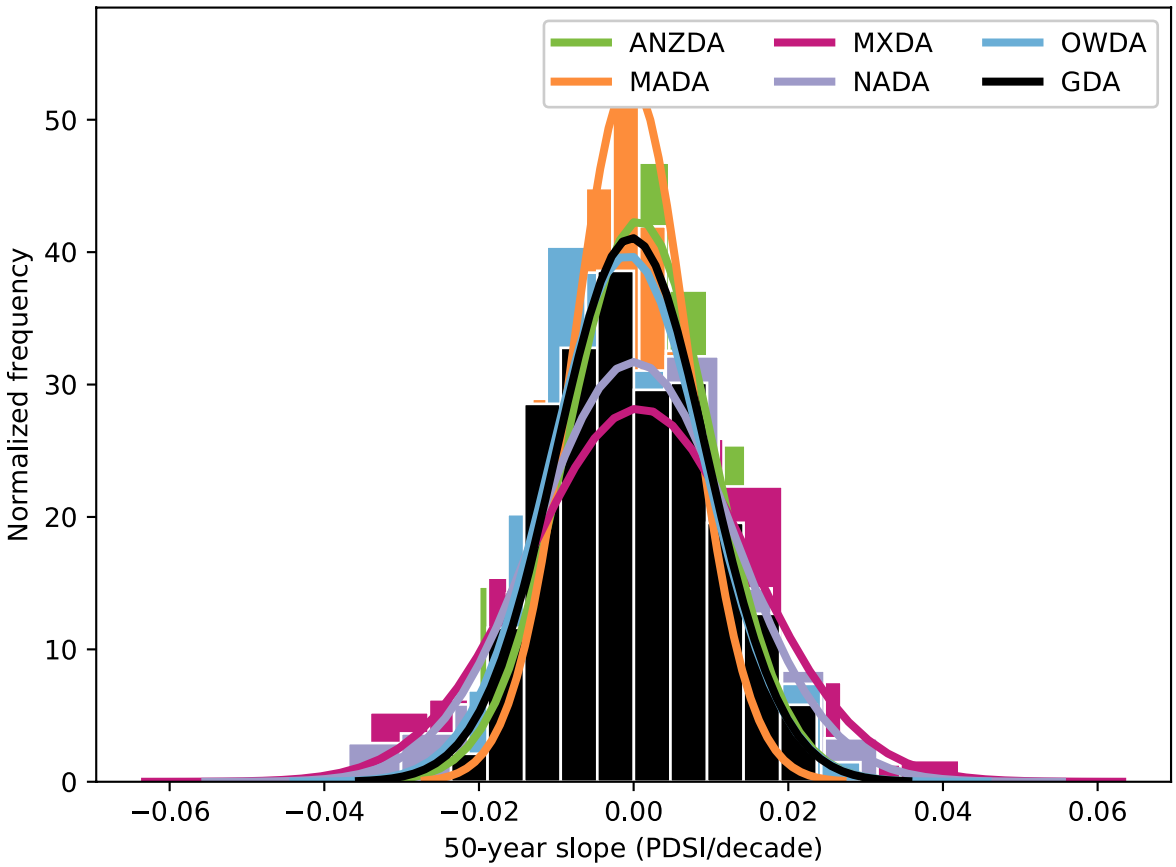

Extended Data Fig. 1 | Noise estimates. Distributions of overlapping (all possible) 50-year trends in the projection of preindustrial reconstructions (1400–1850) of the drought atlas onto the fingerprints shown in Fig. 1a–e. Best-fit Gaussian distributions are overlaid for visual clarity.

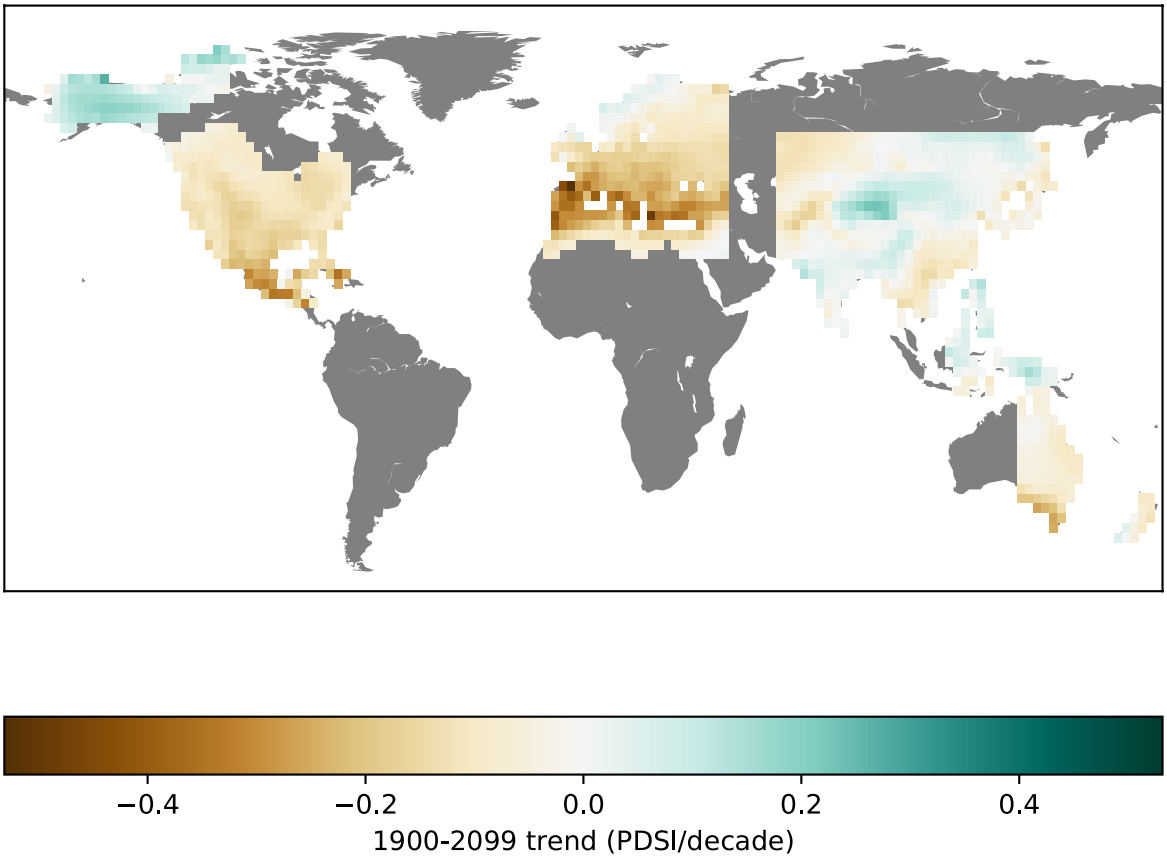

Extended Data Fig. 2 | Trends in the GDA. Linear trends in the multi-model mean CMIP5 historical simulations extended to 2100 with RCP8.5. Trends are calculated for each grid cell using ordinary least-squares regression. The pattern is extremely similar to the fingerprint shown in Fig. 2a, with the pattern correlation exceeding 99%.

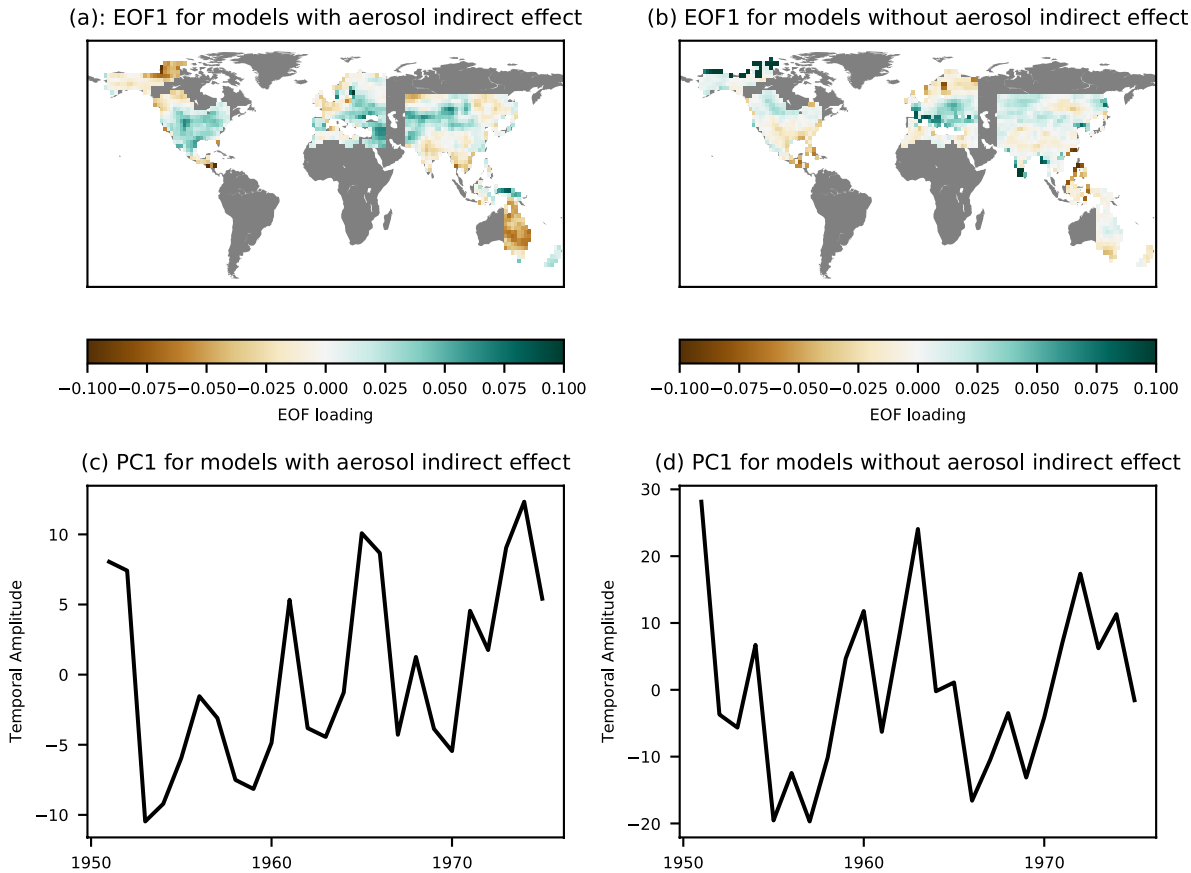

Extended Data Figure 3 | Models with and without aerosol indirect effects. a, **b**, The approximated aerosol fingerprint for models with (**a**) and without (**b**) aerosol indirect effects, defined as the leading EOF of the multi-model average historical simulations over the years 1950–1975. Models are grouped according to the previously reported classifications[39]. **c**, **d**, Associated principal components for the fingerprints shown in **a** and **b**.

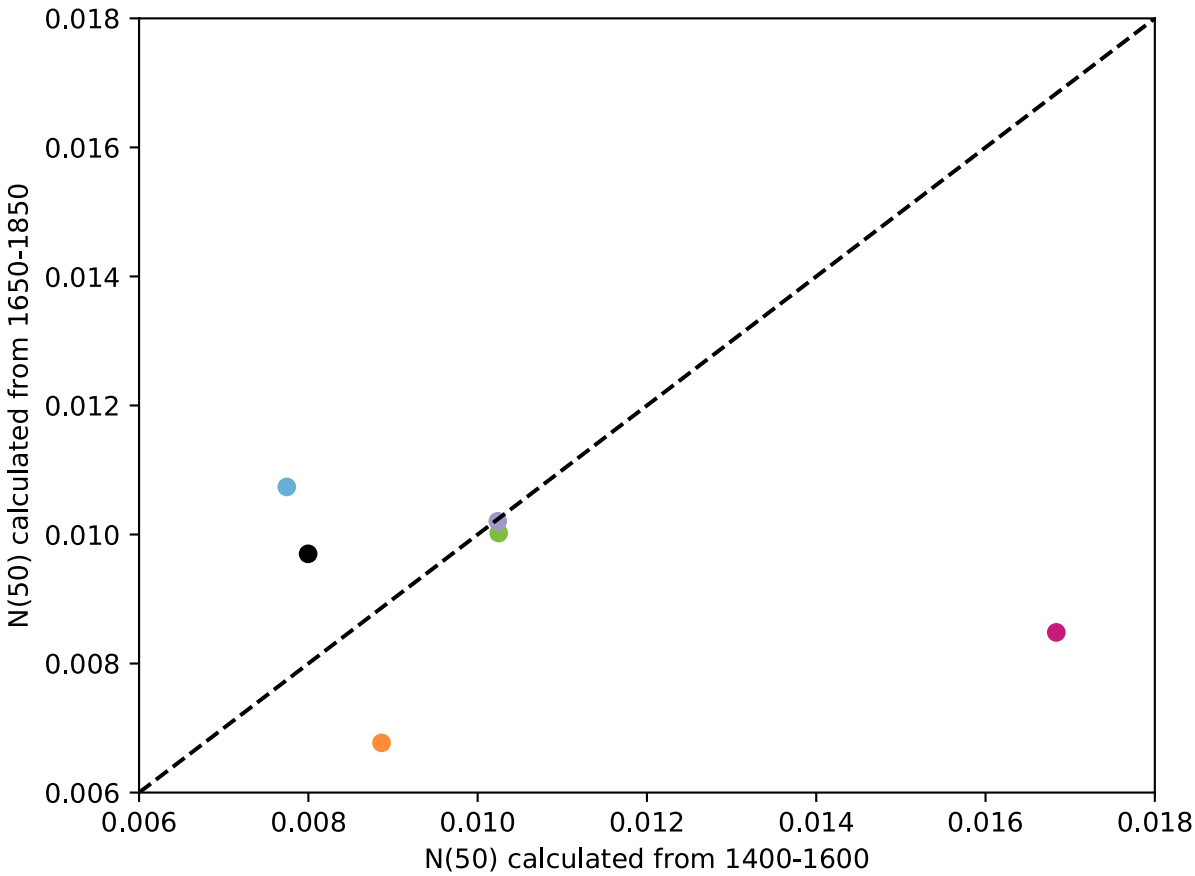

Extended Data Figure 4 | Noise time dependence. The standard deviation of all 50-year trends in projections of the drought atlas for 1400–1850 onto the fingerprints in Fig. 1a–e were calculated from years early (*x* axis) and late (*y* axis) in the preindustrial record. There is no evidence for a systematic difference in noise estimates across drought atlas regions.

Nature Research, brought to you courtesy of Springer Nature Limited (“Nature Research”)

Terms and Conditions

Nature Research supports a reasonable amount of sharing of content by authors, subscribers and authorised or authenticated users (“Users”), for small-scale personal, non-commercial use provided that you respect and maintain all copyright, trade and service marks and other proprietary notices. By accessing, viewing or using the nature content you agree to these terms of use (“Terms”). For these purposes, Nature Research considers academic use (by researchers and students) to be non-commercial.

These Terms are supplementary and will apply in addition to any applicable website terms and conditions, a relevant site licence or a personal subscription. These Terms will prevail over any conflict or ambiguity with regards to the terms, a site licence or a personal subscription (to the extent of the conflict or ambiguity only). By sharing, or receiving the content from a shared source, Users agree to be bound by these Terms.

We collect and use personal data to provide access to the nature content. ResearchGate may also use these personal data internally within ResearchGate and share it with Nature Research, in an anonymised way, for purposes of tracking, analysis and reporting. Nature Research will not otherwise disclose your personal data unless we have your permission as detailed in the Privacy Policy.

Users and the recipients of the nature content may not:

1. use the nature content for the purpose of providing other users with access to content on a regular or large scale basis or as a means to circumvent access control;
2. use the nature content where to do so would be considered a criminal or statutory offence in any jurisdiction, or gives rise to civil liability, or is otherwise unlawful;
3. falsely or misleadingly imply or suggest endorsement, approval , sponsorship, or association unless explicitly agreed to by either Nature Research or ResearchGate in writing;
4. use bots or other automated methods to access the nature content or redirect messages; or
5. override any security feature or exclusionary protocol.

These terms of use are reviewed regularly and may be amended at any time. We are not obligated to publish any information or content and may remove it or features or functionality at our sole discretion, at any time with or without notice. We may revoke this licence to you at any time and remove access to any copies of the shared content which have been saved.

Sharing of the nature content may not be done in order to create substitute for our own products or services or a systematic database of our content. Furthermore, we do not allow the creation of a product or service that creates revenue, royalties, rent or income from our content or its inclusion as part of a paid for service or for other commercial gain. Nature content cannot be used for inter-library loans and librarians may not upload nature content on a large scale into their, or any other, institutional repository.

To the fullest extent permitted by law Nature Research makes no warranties, representations or guarantees to Users, either express or implied with respect to the nature content and all parties disclaim and waive any implied warranties or warranties imposed by law, including merchantability or fitness for any particular purpose.

Please note that these rights do not automatically extend to content, data or other material published by Nature Research that we license from third parties.

If you intend to distribute our content to a wider audience on a regular basis or in any other manner not expressly permitted by these Terms please contact us at

onlineservice@springernature.com
The Nature trademark is a registered trademark of Springer Nature Limited.